Research Square

Preprints are preliminary reports that have not undergone peer review.
They should not be considered conclusive, used to inform clinical practice,
or referenced by the media as validated information.

Gold-Decorated Carbon Dots Carrying Doxorubicin Enhance Tumor Selectivity in A549 Lung Cancer Cells Through Nucleus Targeting and Improved Loading

Iroda Saydullaeva
Samarkand State University named after Sharof Rashidov
Serdar Özçelik
serdarozcelik@iyte.edu.tr
Izmir Institute of Technology

Research Article

Keywords: gold nanoparticles, carbon dots, doxorubicin, drug delivery, cancer selectivity, nuclear targeting

Posted Date: September 3rd, 2026

DOI: https://doi.org/10.21203/rs.3.rs-10467564/v1

License: This work is licensed under a Creative Commons Attribution 4.0 International License.
Read Full License

Additional Declarations: No competing interests reported.

Gold-Decorated Carbon Dots Carrying Doxorubicin Enhance Tumor Selectivity in A549 Lung Cancer Cells Through Nucleus Targeting and Improved Loading

Iroda Saydullaeva[1,2*], Serdar Özçelik[2,*]

[1] Engineering Physics Institute, Samarkand State University, Samarkand, Uzbekistan

[2] Department of Chemistry, Izmir Institute of Technology, Urla-Izmir 35430, Türkiye

* Corresponding author. E-mail: serdarozcelik@iyte.edu.tr or iroda_55@hotmail.com

Iroda Saydullaeva: https://orcid.org/0000-0001-5942-7357

Serdar Özçelik: https://orcid.org/0000-0003-2029-0108

Abstract

Doxorubicin (DOX) efficacy is limited by poor tumor selectivity, multidrug resistance, and cardiotoxicity. Here, to clarify the role of gold decoration in drug delivery, we comparatively studied the selectivity of DOX conjugated to pristine carbon dots (C-dots) and gold-decorated carbon dots (AuNP@C-dots). Using C-dots and AuNP@C-dots (~5.5 nm) prepared in advance, we conjugated DOX via EDC/NHS-mediated coupling and created single-binding (DOX@C-dot) and dual-binding (DOX@AuNP@C-dot) architectures. Spectroscopic characterization confirmed successful DOX conjugation in both systems, with characteristic UV-Vis peaks at 350 nm (C-dot) and 480-500 nm (DOX). Gold decoration enhanced drug loading capacity and conjugate stability relative to pristine C-dots. In A549 lung cancer cells, DOX@C-dot showed minimal cytotoxicity (IC_{50} >2.4 μg/mL), while DOX@AuNP@C-dot was markedly more potent (IC_{50} = 1.7 ± 0.6 μg/mL), a 3.2-fold improvement over free DOX (IC_{50} =5.35 μg/mL)**.** Based on IC_{50} values in A549 versus BEAS-2B cells, DOX@AuNP@C-dot achieved a selectivity index (SI) of 1.72, compared to 1.2 for DOX@C-dot and ~1.0 for free DOX; at the most selective fraction and concentration tested, leading to 3.1-fold preferential cytotoxicity toward cancer cells. Fluorescence microscopy verified that gold decoration improved the selectivity index through nuclear targeting (Pearson coefficient R = 0.67 for DOX@AuNP@C-dot versus 0.42 for DOX@C-dot in A549), a 1.6-fold enhancement. Colony formation assays confirmed superior long-term anti-proliferative effects, with DOX@AuNP@C-dot achieving 61% cancer cell death versus 20% normal cell death. This enhanced performance is attributed to DOX conjugation exploiting gold coordination sites and hydrazone linkages, greater endocytic uptake, pH-triggered release, and carbon dot-mediated nuclear delivery. The architecture leverages carbon dots as nuclear-targeting carriers to deliver DOX-loaded gold nanoparticles into the nucleus of A549 lung cancer cells, a mechanism that in this system addresses both the limited drug-loading capacity of C-dots alone and the inability of AuNPs to access nuclear compartments independently. Together, these results establish that gold-decorated carbon dots improve drug loading, cancer selectivity, and nuclear targeting in this in vitro model, suggesting AuNP@C-dot as a promising nanoplatform warranting further investigation for lung cancer therapy.

Keywords: gold nanoparticles, carbon dots, doxorubicin, drug delivery, cancer selectivity, nuclear targeting

Introduction

The ever-increasing cancer burden in the world makes it necessary to develop new and better therapeutic plans. Although conventional chemotherapeutic medications play a significant role in clinical oncology, they are limited by intrinsic factors, such as low solubility, non-selective tissue distribution, extreme systemic toxicity (e.g., cardiotoxicity), and the ease of multidrug resistance development (MDR) [1, 2]. These vital challenges have resulted in a paradigm shift toward nanomedicine in oncology, where specially engineered nanosystems are applied to enhance the accuracy of drug delivery [3].

Recent developments in cancer nanomedicine focus on multifunctional, stimuli-responsive nanocarriers that can actively and passively target the tumor microenvironment (TME) [4, 5]. Nanoparticles could provide substantial improvements in the effectiveness of therapeutic modalities such as Targeted Therapy, in which the functionalized nanoparticle can effectively target overexpressed receptors, or immunotherapy, by co-delivering anti-immune-modulating factors to enhance the development of anti-tumor immunity or circumvent anti-tumor immune

suppression at the target site [6, 7]. The design of such nanocarriers capitalizes on the enhanced permeability and retention effect (a form of passive targeting) and preferential accumulation in solid tumors, which have leaky vasculature and ineffective lymphatic drainage [7]. The introduction of polymeric, lipid, and inorganic nanoparticles is a significant development that will help enhance combination therapy and theranostics [3].

DOX is a powerful anthracycline drug that has stayed on the leading list of chemotherapeutic agents used in the management of many malignancies (e.g., breast, ovarian, and lung cancers) because of its cytotoxic effect by intercalation of DNA and topoisomerase-II inhibition [8]. Although effective dose-dependent inhibition and rapid elimination, cardiotoxicity severely limits the clinical use of free DOX [9]. DOX's strategic role in nanomedicine is to be the active pharmaceutical ingredient (API), the pharmacological profile of which is dramatically enhanced by its conjugation to a nanoparticle. To be more specific, conjugation of DOX with nanoparticles reduces cardiotoxicity by protecting the drug from non-specific cellular uptake (as with liposomal Doxil) [10], enhances MDR avoidance by circumventing cellular efflux mechanisms [11], and achieves controlled and sustained drug release within the TME [5].

In this work, our primary goal is to enhance the anticancer effectiveness of DOX at minimal doses by conjugating the drug to multi-purpose nanoparticles. Although C-dots and gold nanoparticles have been extensively investigated as individual DOX carriers (over 500 publications combined), hybrid Au-Carbon dot systems remain relatively unexplored, particularly those formed through in situ structural reorganization. Existing strategies for preparing Au–C-dot hybrid nanostructures include in situ reduction (where C-dots act as reductant and stabilizer for AuNP formation) [12], carbonization of AuNP-bound organic ligands [13], multi-step EDC/NHS covalent coupling [14], PAMAM dendrimer-mediated assembly [15], and silica-shell bridging [16]. While each approach has merit, they share critical limitations for nuclear-targeted drug delivery: composite sizes typically exceed 20 nm, precluding efficient traversal of nuclear pores; multi-step protocols reduce reproducibility; and additional linker materials, such as PAMAM, introduce cytotoxicity concerns. Our post-nucleation carbonization approach is mechanistically distinct: pre-synthesized citrate-capped AuNPs are incorporated into the C-dot precursor solution before solvothermal treatment (240°C, 4 h, N_2), during which C-dots form both in the bulk phase and directly on the AuNP surface, establishing covalent Au–S linkages. This process drives structural reorganization of the AuNP precursors, yielding monodisperse hybrid particles of ~5.5 ± 1.3 nm in a single step, without additional reagents or stabilizers. The resulting hybrid preserves the amine-rich C-dot surface chemistry responsible for nuclear targeting while introducing covalently integrated gold coordination sites that substantially enhance drug loading capacity, a key advantage not achievable through conventional post-synthesis conjugation strategies [17].

We employed hydrazone chemistry to functionalize the particle surface for drug conjugation. Hydrazone linkages are well established in the literature for stability at physiological pH (7.4) and for accelerated hydrolysis under mildly acidic conditions (pH 5.0–6.5), such as those found in endosomal/lysosomal compartments [12]. This pH sensitivity was a deliberate design rationale to enable intracellular drug release, rather than a release profile we directly measured. Consistent with this expected behavior, we observed potent, dose-dependent cytotoxicity and DOX accumulation in the nucleus of A549 cells, which is compatible with, though does not on its own confirm, pH-triggered release inside the cell. Following purification by gel filtration, the conjugates' properties and drug-loading efficiency were characterized using optical spectroscopy and molecular weight analysis, revealing that gold decoration enables up to a 5-fold enhancement in molar loading capacity, with peak values of approximately 220 DOX molecules per AuNP@C-dot compared with 46 molecules for pristine C-dots. Biological validation was conducted in A549 lung cancer cells and BEAS-2B normal lung epithelial cells to assess both therapeutic efficacy and cancer cell selectivity. Our results demonstrate that the dual binding architecture—comprising gold coordination sites—achieves superior drug-loading capacity and enhanced cancer cell selectivity (3.1-fold versus normal cells) compared to pristine C-dots. By leveraging the synergistic properties of gold-carbon hybrid nanostructures and pH-triggered intracellular release, we present a versatile chemotherapeutic platform with potential for multimodal therapy, including radiotherapy, photodynamic therapy, and photothermal therapy, offering highly controlled and selective delivery of chemotherapeutic agents to the nucleus.

Materials and Methods

Materials

Doxorubicin was purchased from Adooq Bioscience. N-Hydroxysuccinimide (NHS) and N-(3-dimethylaminopropyl)-N′-ethylcarbodiimide hydrochloride (EDC) were obtained from Thermo Fisher Scientific.

Fetal bovine serum (FBS), penicillin-streptomycin, L-glutamine, trypsin-EDTA, Dulbecco's Modified Eagle Medium (DMEM), and Roswell Park Memorial Institute (RPMI) 1640 medium were purchased from GIBCO. 4-Hydrazinobenzoic acid (HBA), citric acid (99.9%), hydrogen tetrachloroaurate (III) trihydrate (99.0%), and sodium borohydride (99.0%) were obtained from Sigma-Aldrich. Thiourea (99.9%) was purchased from Alfa Aesar, and ethylenediamine from Merck. Ultrapure water from a Millipore purification system was used in all experiments.

Synthesis of C-dots and AuNP@C-dots Hybrid Nanostructures

C-dots were synthesized via solvothermal reaction of citric acid and thiourea (molar ratio 1:5.3) in DMF at 240°C for 4 hours under a nitrogen atmosphere, as previously reported [17]. The resulting product was purified by ethanol-assisted centrifugation, and the dried particles were redispersed in water, DMF, or DMSO, depending on the application requirements.

AuNP@C-dots were prepared by incorporating pre-synthesized citrate-capped AuNPs (40 nm diameter, 1.0×10^{10} particles/mL) into the C-dot precursor solution before thermal treatment. The mixture was subjected to the same solvothermal conditions (240 °C, 4 h, N_2 atmosphere), followed by ethanol-assisted purification and freeze-drying. The final hybrid nanoparticles were redispersed in appropriate solvents for further use.

Conjugation of DOX to C-dots and AuNP@C-dots

DOX was conjugated to C-dot and AuNP@C-dot particles via hydrazone bonding chemistry followed by EDC/NHS covalent attachment [18, 19]. Due to the limited solubility of C-dot-based particles in aqueous buffer, a stock solution of C-dots or AuNP@C-dots was first prepared by dissolving the material in 0.2% (v/v) DMSO, followed by dilution with sodium bicarbonate buffer. For conjugation, 800 µg of C-dots or AuNP@C-dots was diluted in 200 µL PBS. Then, 400 µL of 4-hydrazinobenzoic acid in DMSO (9.5 mg/mL) was added, followed by 5 µL of acetic acid to catalyze hydrazone formation. The mixture was stirred in the dark at room temperature for 72 hours. After incubation, 100 µL of EDC in PBS (17.7 mg/mL) was added and stirred for 30 minutes. Subsequently, 100 µL of NHS in PBS (10.68 mg/mL) was added, and the solution was stirred for another 30 minutes. DOX (4.72 mg/mL in DMSO) was then added to the mixture and allowed to react overnight under gentle stirring at room temperature.

Purification: Gel Filtration Chromatography

The DOX-conjugated nanoparticles (DOX@C-dot and DOX@AuNP@C-dot) were purified using gel filtration chromatography with Sephadex G-25 (Sigma-Aldrich, Germany). Briefly, a glass column (1×20 cm) was packed with Sephadex G-25 resin to a bed volume of approximately 15 mL, giving a height of approximately 19 cm, equilibrated with phosphate-buffered saline (PBS, pH 7.4). Samples were loaded at a volume not exceeding 10% of the bed volume (~1.5 mL). Elution proceeded under gravity flow at an approximate flow rate of 0.5–0.6 mL/min. The relevant fractions (1.5 mL each) were collected and stored at 4 °C for further characterization.

Optical spectroscopy

UV-Vis absorption and photoluminescence spectra of the samples were recorded using an Edinburgh Instruments FS5 spectrofluorometer. The quantification of DOX loading was determined via UV–Vis spectroscopy. The mass concentrations were calculated via the Beer–Lambert law:

$$c = \frac{A}{\epsilon_m \cdot l}$$

where A is the absorbance at the respective wavelength, ε_m is the mass extinction coefficient (13.93 $L\cdot g^{-1}\cdot cm^{-1}$ for C-dots [16], and 11.5 $L\cdot g^{-1}\cdot cm^{-1}$ for DOX [17], and l is the cuvette path length (1 cm). The DOX loading efficiency (DLE) was then calculated as [12]:

$$DLE(\%) = \frac{mass\ o\ f\ DOX}{mass\ of\ C-dots\ +\ mass\ of\ DOX} \times 100$$

This quantification method allowed precise determination of the relative amounts of C-dots and DOX in the conjugates from their UV–Vis absorbances, facilitating estimation of drug loading and conjugation ratios in the hybrid nanostructures.

Cell Culture

A549 and BEAS-2B cell lines were purchased from ATCC and were propagated as recommended using DMEM/F-12 and RPMI medium, respectively, supplemented with 10% FBS, L-glutamine (2 mM), penicillin (100 U/mL), and streptomycin (100 mg/mL). All experiments were conducted using cells grown in a humidified incubator containing 5% CO2 at 37 °C.

Colony Formation Assay

Cells (1.5 × 103 cells/well) were seeded on 6-well plates and incubated at 37 °C in 5% CO2 conditions for 24 h. Then, cells were incubated for 24 h with various amounts of treatments. After that, the cell medium was replaced with a fresh medium, eliminating DOX-conjugated nanoparticles that were not internalized. After seven days of incubation, each well was fixed and stained using crystal violet solution (0.5% crystal violet, 1% formaldehyde, 1% methanol, and 1x PBS) at 25°C for 30 min. The stained cells were gently washed with water and then air-dried at room temperature. The number of colonies was quantified using the ImageJ colony counting plug-in (version 1.53f51; National Institutes of Health, Bethesda, MD, USA). Experiments were repeated at least three times.

Determination of Cytotoxicity by MTT Assay

MTT (3-(4,5-dimethylthiazol-2-yl)-2,5-diphenyltetrazolium bromide) assay was performed to evaluate cell viability following the nanoparticle treatment. Cells were plated at a density of 4500 cells per well in flat-bottom 96-well plates and allowed to grow and attach overnight (~24 h) before treatment. Cells were then exposed to DOX@C-dot and DOX@AuNP@C-dots at different concentrations, suspended in an appropriate medium according to cell line, for a single continuous 24 h treatment period. Each concentration was tested in five technical replicate wells per biological repeat, across at least three independent biological replicates. Following incubation, the cell medium was replaced with 10.0 µL of MTT solution (5 mg/mL), and the plates were incubated at 37 °C for 4 hours. Afterwards, 100 µL DMSO solvent was added to dissolve the formazan crystal at room temperature. The plates were shaken for 15 min to solubilize formazan crystals. The absorbance was measured using a spectrophotometer (with a microplate reader) at 570 nm.

Fluorescence Microscopy

The cells were grown in the T-25 flask. The day before treatment, 2×10^5 cells per well were seeded onto glass coverslips in a 6-well plate. The following day after planting, the cell density was confirmed using an optical microscope. Afterward, the cells were incubated with the DOX-conjugated particle suspensions for 6 hours. At the time of analysis, cells on coverslips were rinsed with PBS and fixed with methanol at 4 oC for 20 min. Next, the coverslips were picked up and left to air dry. 10 µL of 1.0 µg/mL DAPI was dropped on the coverslip and placed on a slide to stain nuclei. Subsequently, the cells on the coverslips were imaged immediately using a Zeiss AxioZoom V.16 microscope with DAPI (Zeiss filter set 49 HE), green and red (Zeiss filter sets 38 HE and 63 HE) filter sets for fluorescence imaging, as well as bright-field and dark-field contrast methods.

Statistical analysis

All experiments were performed in at least three independent biological replicates ($n \geq 3$). Data are presented as mean ± standard deviation (SD) or mean ± standard error of the mean (SEM) as indicated in the figure legends. Statistical analyses were performed using GraphPad Prism version 10.0 (GraphPad Software, San Diego, CA, USA). Comparisons between multiple groups were analyzed using one-way analysis of variance (ANOVA) followed by Tukey's post-hoc test for multiple comparisons. Dose-response curves and IC_{50} values were determined by four-parameter logistic (4PL) regression curve fitting using the 'drc' package (version 3.0-1) in R statistical environment (version 4.3.0). The selectivity index (SI) was calculated as the ratio of IC_{50} values (SI = IC_{50}_normal cells / IC_{50}_cancer cells), with SI > 1 indicating preferential toxicity toward cancer cells. Pearson's correlation coefficients were calculated using ImageJ (version 1.53f51, National Institutes of Health) with the Coloc2 plugin to quantify

colocalization between DAPI and drug-conjugate fluorescence signals. Statistical significance levels are indicated as *p < 0.05, **p < 0.01, ***p < 0.001, and ****p < 0.0001.

Results

Analysis of Drug Conjugation and Purification

The C-dot and AuNP@C-dot particles were prepared by following the method we developed recently [13]. Briefly, the particles have an average diameter of 5.5 $\pm$ 1.3 nm, having chemical composition of carbon, oxygen, nitrogen, and sulfur atoms (w/o 40, w/o 30, w/o 10, w/o 10, respectively) for C-dot, in addition to containing gold (w/o 0.4) for AuNP@C-dot. The synthesis of the drug-particle conjugates, DOX@C-dot and DOX@AuNP@C-dots conjugates, was optimized based on the previously reported method by Hettiarachchi et al. [14], utilizing HBA and EDC/NHS chemistry to attach DOX to the particles. Following the conjugation reaction, the crude products were subjected to size-exclusion chromatography for purification. The collected fractions were then systematically characterized using UV-Vis absorption, Photoluminescence (FL), and Fourier-transform infrared (FTIR) spectroscopies to confirm the successful attachment of the linkers and DOX to the nanoparticles. The spectroscopic findings validating the formation and purification of the conjugate are presented below.

The UV-Vis absorption spectra of the fractionated samples (each fraction in a volume of 1.5 mL) provide clear evidence of successful DOX conjugation and subsequent purification. For both the DOX@C-dot and DOX@AuNP@C-dot conjugates, the early chromatographic fractions consistently exhibited high absorbance signals of DOX, which progressively decreased in the following fractions. This trend indicates the efficient size-exclusion separation of the larger, conjugated nanoparticles (approximated as 10 nm, based on DLS and TEM measurements of AuNP@C-dot particles) from the smaller, unbound/free DOX (predicted size of 1 nm) and other reaction byproducts. Full spectra of all fractions together with free DOX are available in the supplementary materials, Figure S2.

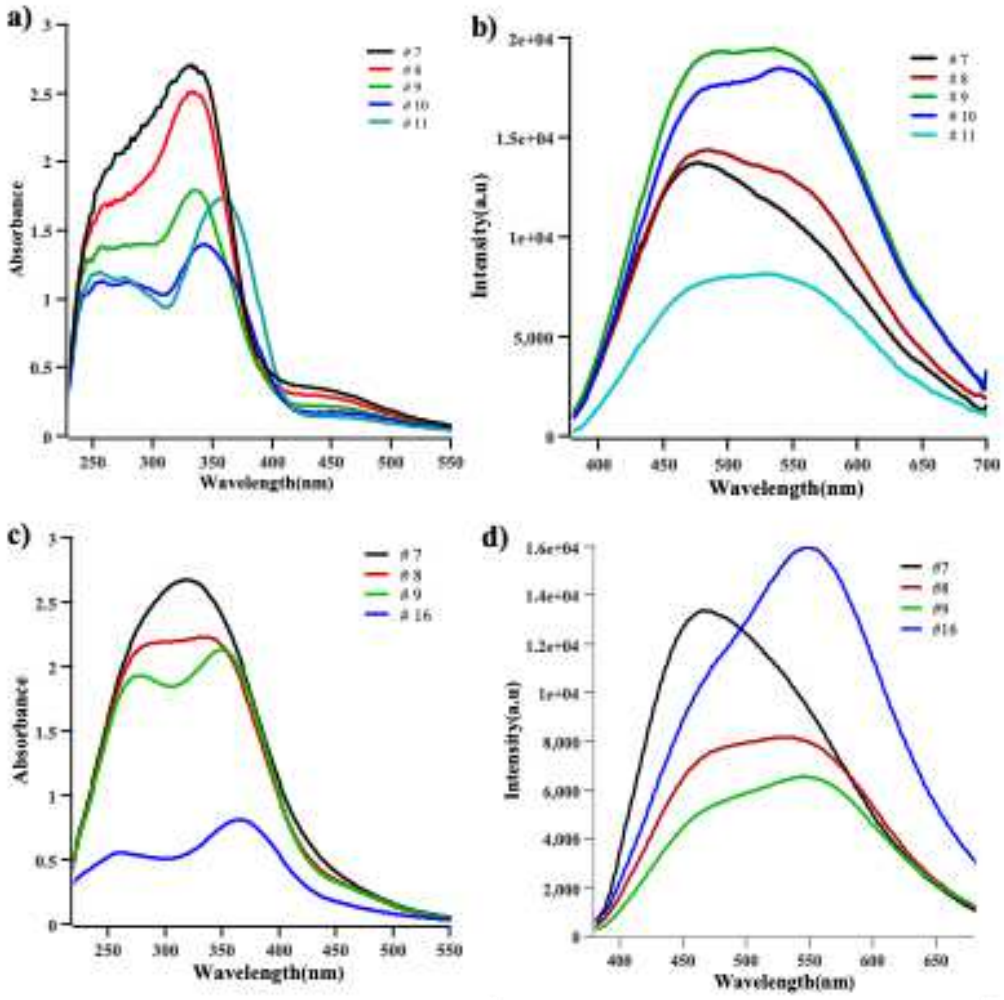


Fig 1 Spectroscopic Analysis of DOX-Nanoparticle Conjugates: UV-Vis Absorbance and Photoluminescence Spectra of Representative Fractions. (a, c) UV–Vis absorbance and (b, d) photoluminescence emission spectra of the selected size-separated fractions obtained after gel chromatography purification. Panels (a) and (b) (top row) correspond to the purified DOX@C-dot conjugate, while panels (c) and (d) (bottom row) correspond to the DOX@AuNP@C-dot hybrid conjugate. The data confirm the successful formation and purification of the Dox-loaded nanoparticles from unreacted components. The fraction numbers are shown in the insets.

Spectral Characterization of the Conjugates

Figure 1 represents UV-Vis absorption and photoluminescence spectra of representative purified fractions of DOX-nanoparticle conjugates. The fractions 7 to 11 of DOX@C-dot showed distinct absorbance peaks around 350 nm, characteristic of the C-dot core, alongside pronounced shoulders at 480–500 nm attributed to DOX spectral features, suggesting covalent bond formation of DOX to the nanoparticle. These combined absorption features clearly indicate the coexistence of both C-dot and DOX components within these fractions, consistent with effective conjugate formation. Photoluminescence (PL) spectra recorded under 350 nm excitation further corroborated these findings. The emission profiles exhibited a moderate red shift, broadening, and significant fluorescence quenching relative to non-conjugated C-dots, indicative of effective covalent attachment of DOX, which partially suppressed the C-dot emission. In contrast, later-eluting fractions showed diminished DOX absorbance signals and a relative recovery of PL intensity, suggesting the presence of either residual free C-dots or unbound DOX molecules.

A similar successful trend was observed for the DOX@AuNP@C-dots system. The fractions 7 to 9 exhibited combined absorption features of both the C-dots and DOX, confirming that AuNP decoration did not impede the

conjugation efficiency. Notably, the PL spectra of these DOX@AuNP@C-dot conjugates exhibited even more pronounced PL quenching than the C-dot-DOX samples. This enhanced quenching is likely due to additional nonradiative energy transfer or plasmonic interactions between the adjacent AuNP cores and the fluorophores (both the C-dot and DOX). Later fractions (e.g., fraction 16) were dominated by unmodified AuNP@C-dot, showing strong native PL with negligible DOX-related absorbance, thus signifying complete separation of DOX from the conjugated species.

FTIR spectroscopic analysis

The FTIR features associated with C-dots and AuNP@C-dots confirm their covalent attachment, previously proven, along with thorough spectral and structural characterization [13]. In this work, the focus is on the IR spectral alterations arising from the DOX conjugation. Compared with their bare counterparts, both DOX@C-dot and DOX@AuNP@C-dot did not exhibit new absorption bands(Fig. 2); however, subtle yet consistent intensity changes were observed in the fingerprint region (~1700–1000 cm^{-1}). A modest enhancement in the amide I/II region (~1650–1540 cm^{-1}) and slight modifications in the O–H/N–H stretching envelope (~3300 cm^{-1}) support the formation of hydrazone-linked DOX on the nanoparticle surfaces. Minor attenuation around 1050 cm^{-1} further indicates participation of surface C–O/C–O–C groups in the coupling reaction. Since functional groups and parts of DOX, hydrozinobenzoic acid, and EDC/NHS resemble the groups existing in C-dots and on the surface of AuNPs, it is anticipated that the FTIR spectra remain similar, along with some intensity modifications. Although the overall spectral profiles represent resemblance to the pristine particles, these reproducible intensity variations collectively advocate the successful conjugation of DOX onto both C-dot and AuNP@C-dot particles.

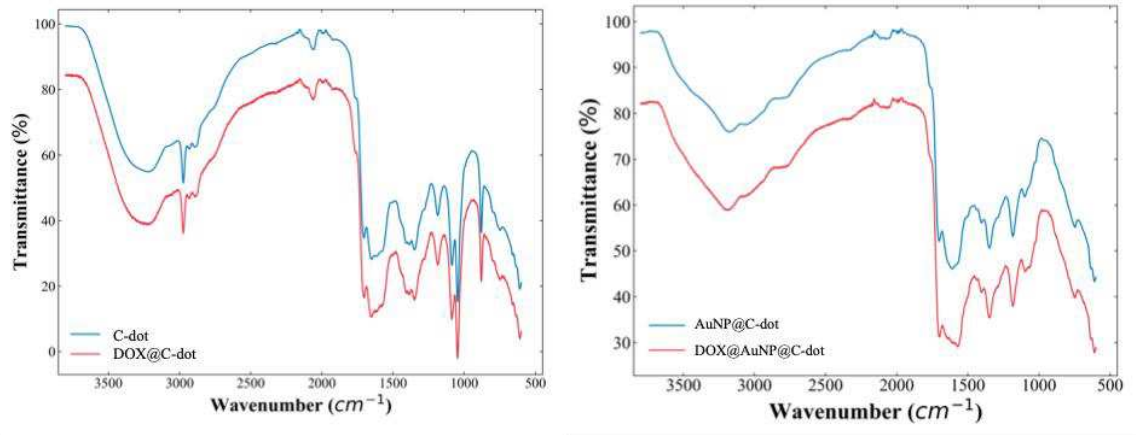


Fig.2 FTIR spectra of unconjugated and DOX-conjugated C-dots (left) and AuNP@C-dots (right), showing fingerprint-region shifts indicative of successful drug binding.

Distribution and Efficiency of DOX Conjugation Across Fractions

The DOX-nanoparticle conjugates were quantitatively characterized using both a dialysis-based method and gel chromatography-based fractionation to determine drug loading efficiency (DLE) and conjugate stability. Initially, the conjugate was purified by dialysis. The reaction mixture was transferred into a Slide-A-Lyzer™ Dialysis Cassette (Thermo Fisher Scientific, 2K MWCO, 3 mL) and dialyzed against 40 mL of deionized water for 24 hours under continuous stirring. During this process, unreacted DOX diffused into the external medium. The concentration of dialyzed, unbound DOX in the external solution was measured to be 1.28 mg/mL by UV-Vis spectroscopy. Based on this value, the DLE was calculated as 72.88%. The conjugate mixture within the dialysis cassette could not be effectively recovered, most likely due to substantial adsorption of the conjugates onto the membrane walls. The gel filtration chromatography was subsequently employed as an alternative purification method. The fractions obtained by the gel chromatography were used to evaluate the conjugation profile of DOX to C-dots and AuNP@C-dots employing quantitative analysis based on absorbance measurements at 350 nm and 480 nm, corresponding to C-dots and DOX, respectively. Component concentrations in each fraction were quantitatively determined using the Beer–

Lambert law using the molar extinction coefficients for DOX and C-dots obtained from the literature to ensure consistency and accuracy in spectroscopic analysis [16, 17]. DLE and C-dot/DOX mass ratios were subsequently calculated. Table 1 presents the fractions in which conjugation is believed to predominate, while the complete set of fractions is available in the supplementary materials. Multiple fractions were profiled, rather than assuming a single elution peak of conjugated product, because gel filtration separates primarily by hydrodynamic size and does not by itself distinguish fully conjugated particles from loosely associated or co-eluting free DOX; the early, DOX-rich fractions in particular can overstate apparent loading if taken alone. Profiling the full elution series allowed us to identify the mid-to-late fractions (F7-F10) in which DOX content and particle mass ratio stabilize together, and we treat this stable window — rather than any single fraction or an unweighted average across all fractions — as the representative conjugate population used for downstream biological testing.

Table 1. Quantitative Analysis of DOX Loading onto Carbon Dots across Various Sample Fractions.

Sample	A350	A480	C-dot (mg/L)	DOX (mg/L)	Mass C-dot (µg)	Mass DOX (µg)	DLE (%)	C-dot/Dox ratio
F.7	2.44	0.25	0.18	0.02	175.34	21.63	11.00	8.11
F.8	2.22	0.21	0.16	0.02	159.26	18.63	10.50	8.55
F.9	1.59	0.17	0.11	0.02	114.01	14.79	11.50	7.71
F.10	1.36	0.15	0.10	0.01	97.94	12.73	11.50	7.70
F.11	1.69	0.12	0.12	0.01	120.94	10.35	7.90	11.68

Quantitative evaluation of all chromatographic fractions revealed a distribution of DOX and nanoparticle content, calculated as defined in the methods section. As observed in both the DOX@C-dot and DOX@AuNP@C-dot systems, the initial fractions exhibited elevated DLE values; these fractions also contained a very low quantity of total conjugates, suggesting limited relevance to the bulk product. However, the highest conjugate yield was found in mid to late fractions, particularly those corresponding to fractions 7-10, which were initially predicted to contain the main conjugate population. These fractions displayed a balanced profile of DOX content (approx. 10–13% DLE) and stable conjugate mass ratios (~8–10), which means that for every 1 mg of DOX, there are 8–10 mg of C-dots present in those fractions, suggesting that these segments comprise the most representative population of firmly bound DOX-conjugated nanoparticles.

It should be noted that the value of 32.5% reported previously represents a simple arithmetic mean across all 16 collected fractions, including early fractions (F3–F5) that contain high DOX absorbance signals attributable to loosely associated or free DOX co-eluting with larger aggregates rather than stable conjugates. The biologically relevant DLE for the pooled active fractions (F7–F10), calculated as the ratio of total DOX mass to total combined mass in those fractions, is 11.1%, consistent with the individual fraction values reported in Table 2.

Table 2. Quantitative Analysis of DOX Loading and Calculated DLE for DOX@AuNP@C-dot Fractions

Sample	A350	A480	AuNP@C-dot(mg/L)	Dox (mg/L)	Mass AuNP@C-dot (µg)	Mass Dox (µg)	DLE (%)	AuNP@-dot/Dox ratio
F.7	2.40	0.24	0.17	0.02	172.52	21.04	10.87	8.20
F.8	2.17	0.22	0.16	0.02	155.61	19.34	11.06	8.05
F.9	2.13	0.22	0.15	0.02	152.80	19.32	11.23	7.91
F.10	2.05	0.21	0.15	0.02	147.41	18.63	11.22	7.91
F.11	2.06	0.20	0.15	0.02	148.01	17.35	10.49	8.53

To provide a more comprehensive understanding of the drug loading characteristics, mass-based ratios were converted to molar ratios for both DOX@C-dot and DOX@AuNP@C-dot particles (Table S2/S4). The molecular weight equivalent for nanoparticles was calculated from their physical dimensions, assuming spherical geometry. For a particle with diameter d (nm) and density ρ (g/cm³), the mass per particle was calculated as: $m = \rho \times (4/3)\pi(d/2 \times 10^{-7})^3$ [18], where the factor 10^{-7} converts nanometres to centimetres. The molecular weight equivalent was then obtained by multiplying the mass per particle by Avogadro's number. For DOX@C-dot, TEM analysis showed the C-dot dimension of approximately 5.5 nm. Using an estimated density of 1.8 g/cm³ based on the amorphous nature

of carbon dots and the presence of heteroatoms (N, O, S) from the citric acid-thiourea synthesis, the calculation yielded a mass of 1.57×10^{-19} g per particle and a MW of 9.44×10^{4} g/mol. Molar ratio analysis of gel filtration fractions revealed 10-46 DOX molecules bound per C-dot particle (detailed calculations for all fractions are provided in the supplement). For DOX@AuNP@C-dots, TEM analysis confirmed that the hybrid particles maintain similar dimensions (average of 5.5 nm) to pristine C-dots, indicating that the gold nanoparticles underwent structural reorganization during the high-temperature solvothermal synthesis (240 °C, 4 h), resulting in gold atoms or small gold clusters incorporated within or decorated on the carbon dot matrix. EDX analysis confirmed the presence of gold at 0.39 wt% in the hybrid structure [13]. Accounting for the slightly higher density due to gold incorporation (calculated as 1.87 g/cm³ from the weighted contribution of carbon and gold components), the hybrid particle mass was calculated as 1.63×10^{-19} g and MW as 9.80×10^{4} g/mol. Molar ratios across gel filtration fractions ranged from 20 to 220 DOX molecules per AuNP@C-dot particle. This 5-fold enhancement in drug loading capacity of DOX@AuNP@C-dots compared to DOX@C-dots demonstrates the beneficial effect of gold incorporation, where the gold clusters provide additional coordination sites for DOX binding (through Au-amine and Au-carbonyl interactions) that complement the pH-sensitive hydrazone linkages formed at the C-dot surface, resulting in superior drug loading while maintaining the advantageous size for cellular uptake and nuclear targeting.

Table 3. Comparative Loading Efficiencies: Molar Ratios of DOX per Particle

Particle	Particle Size	MW (g/mol)	DOX Loading
DOX@C-dot	5.5 nm	9.44×10^{4}	10-46 DOX/particle
DOX@AuNP@C-dot	5.5 nm	9.80×10^{4}	20-220 DOX/particle
Enhancement	Same size	1.04x heavier	~5× higher

Based on this quantitative assessment (Table 3), the initial fractions may be enriched by free or loosely associated DOX. In contrast, the mid-range fractions represent a more realistic composition of the final conjugate, striking a balance between effective loading and structural stability. Indeed, the higher mass of C-dot–DOX material in these fractions, alongside sustained DLE, supports the notion that the fractions 7–10 likely constitute the drug particle conjugates suitable for downstream biological evaluation.

Cell viability

Cytotoxic Effect of DOX on A549 Cells

The cytotoxic effects of DOX on the viability of A549 lung cancer cells were evaluated using both MTT and CFA assays. As shown in Figure 3, DOX treatment resulted in a dose-dependent decrease in A549 cell viability, with an experimentally determined IC50 value of 5.35 μg/mL (≈9.22μM). This result is consistent with the range of IC_{50} values previously reported in the literature. While reported values vary significantly—ranging from as low as 8.64 nM (0.005 μg/mL) for 72-hour exposures [19] to as high as 71 μM (41.2 μg/mL) for 24-hour treatments [20], these discrepancies are primarily attributed to differences in experimental conditions, seeding densities, and assay durations(Fig. 3b).

The long-term impact of DOX was further confirmed by the CFA(Fig. 3a), which demonstrated a significant reduction in clonogenic survival of A549 cells as DOX concentration increased. At 1000 nM (≈ 0.54 μg/mL), DOX almost completely abrogated colony formation, highlighting its potent and sustained anti-proliferative activity against A549 cells. These findings emphasize DOX's established efficacy as a chemotherapeutic agent and provide a critical baseline for evaluating the improved delivery and enhanced toxicity of the drug- nanoparticle conjugates with reduced quantity.

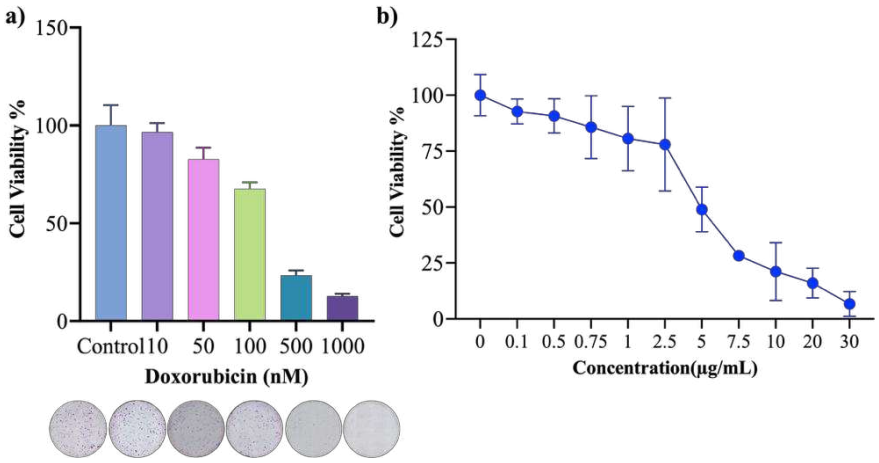


Fig. 3 DOX inhibits the growth and survival of A549 lung cancer cells. (a) Representative plate images of the CFA showing a dose-dependent reduction in the number of colonies after treatment with Doxorubicin for 8 days. Statistical significance was determined by one-way ANOVA (****$p < 0.0001$). (b) Cell viability in the MTT Assay was measured after 24 h of treatment. The calculated IC_{50} value for DOX in this cell line was 5.35 µg/mL. Statistical significance was determined by one-way ANOVA (*$p < 0.05$). Data represent the mean ± SD of three independent experiments.

Assessment of Cell Viability and Metabolic Activity of the Conjugates by MTT Assay

To assess the impact of drug-nanoparticle conjugates on DOX's efficacy and selectivity, the cytotoxicity of DOX@C-dot and DOX@AuNP@C-dot fractions was evaluated in A549 lung cancer cells versus BEAS-2B normal lung epithelial cells using the MTT assay (Fig. 4). Two volumes (20 µL and 40 µL) of each fraction were tested to assess dose-dependent outcomes. Four-parameter logistic curve fitting revealed distinct IC_{50} values for DOX@AuNP@C-dots: 1.692 ± 0.633 µg/mL for A549 cells ($R^2 = 0.8161$) and 2.910 ± 0.396 µg/mL for BEAS-2B cells ($R^2 = 0.8691$). The calculated selectivity index (SI = IC50_BEAS-2B / IC50_A549) of 1.72 indicates that the nanoconjugate exhibits 1.7-fold preferential toxicity toward cancer cells, representing good cancer selectivity for a chemotherapeutic agent.

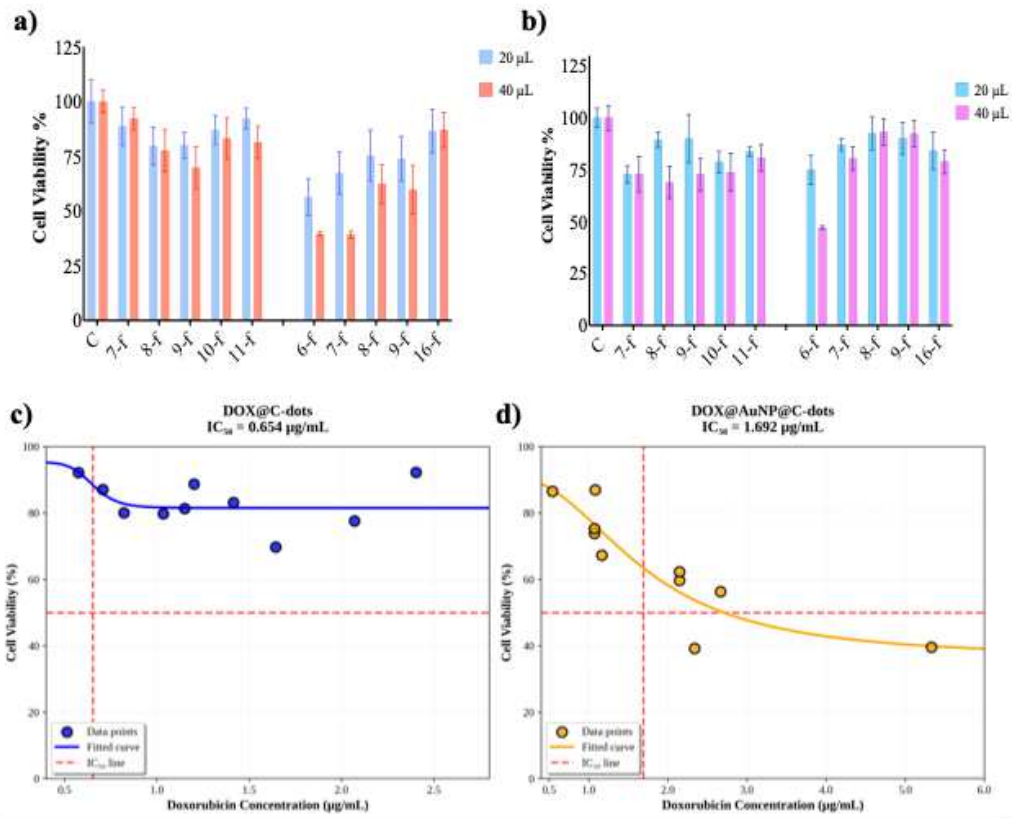


Fig. 4 Cytotoxicity and Dose-Response Analysis of DOX conjugates. Cell viability of A549 (a) and BEAS-2B (b) cells after treatment with DOX@C-dot (left clusters) and DOX@AuNP@C-dot (right clusters) at indicated volumes (20 and 40 µL). Data represent the mean ± SD from three independent experiments. Statistical significance determined by one-way ANOVA (****$p < 0.0001$). (c, d) Dose-response curves and IC_{50} determination against A549 lung cancer cells for (c) DOX@C-dot and (d) DOX@AuNP@C-dot. Solid lines represent four-parameter logistic curve fits, with dashed red lines indicating the 50% viability threshold.

Concentration-dependent analysis (Fig. 5) revealed that selectivity varied across different fractions. The fraction-7 at 2.338 µg/mL demonstrated particularly strong selectivity, reducing A549 viability to 39.22 ± 0.84% while maintaining BEAS-2B viability at 80.41 ± 2.82%, corresponding to a 3.1-fold selectivity ratio at this concentration. The fraction-6, while highly potent at 5.331 µg/mL (reducing A549 to 39.57 ± 0.44% and BEAS-2B to 47.12 ± 0.44%), showed reduced selectivity (1.1-fold) at this higher dose.

In contrast, DOX@C-dot demonstrated minimal cytotoxicity in both cell lines, with viabilities remaining above 68% across all tested concentrations, resulting in no discernible cancer selectivity. This difference underscores the critical role of gold nanoparticles in achieving both enhanced cytotoxicity and cancer-selective delivery.

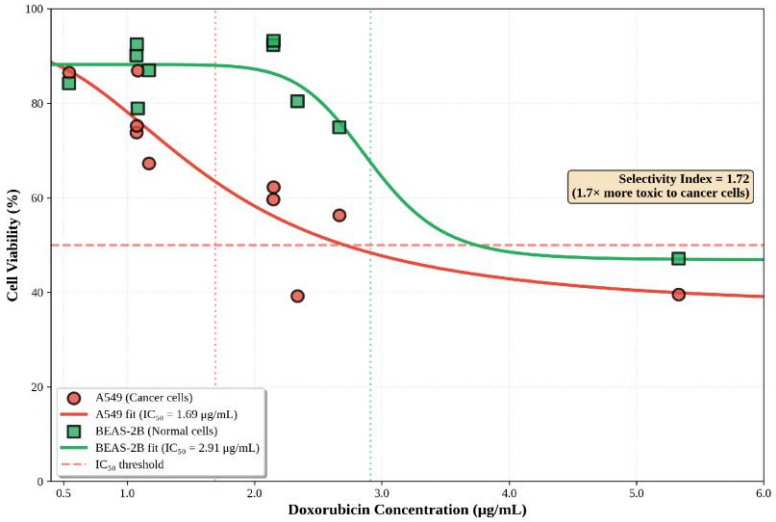


Fig. 5 Cancer cell selectivity of DOX@AuNP@C-dot. Dose-response curves comparing cytotoxicity in A549 versus BEAS-2B cells after 24h treatment. Data points represent mean ± SEM (n=4). Solid lines show four-parameter logistic curve fits. The dashed line indicates a 50% viability threshold. Dotted vertical lines mark respective IC50 values. The nanoconjugate demonstrates good cancer selectivity with a selectivity index of 1.72, indicating 1.7-fold preferential toxicity toward cancer cells.

Long-term Anti-proliferative Effects of the Conjugates by CFA

Colony formation assays demonstrated that DOX@C-dot and, specifically, DOX@AuNP@C-dot conjugates exert substantial toxicity, reducing the proliferation of cancerous A549 cells compared to normal BEAS-2B cells (Fig. 6 and 7). In A549 cells, these conjugates induce a marked, dose-dependent reduction in colony formation, sometimes nearly abolishing it, when treated with fractions 7 and 16 (labelled as F7 and F16), with viability dropping to as low as 10% of the untreated controls. This demonstrates a potent cytotoxic / chemo-therapeutic activity toward cancer cells.

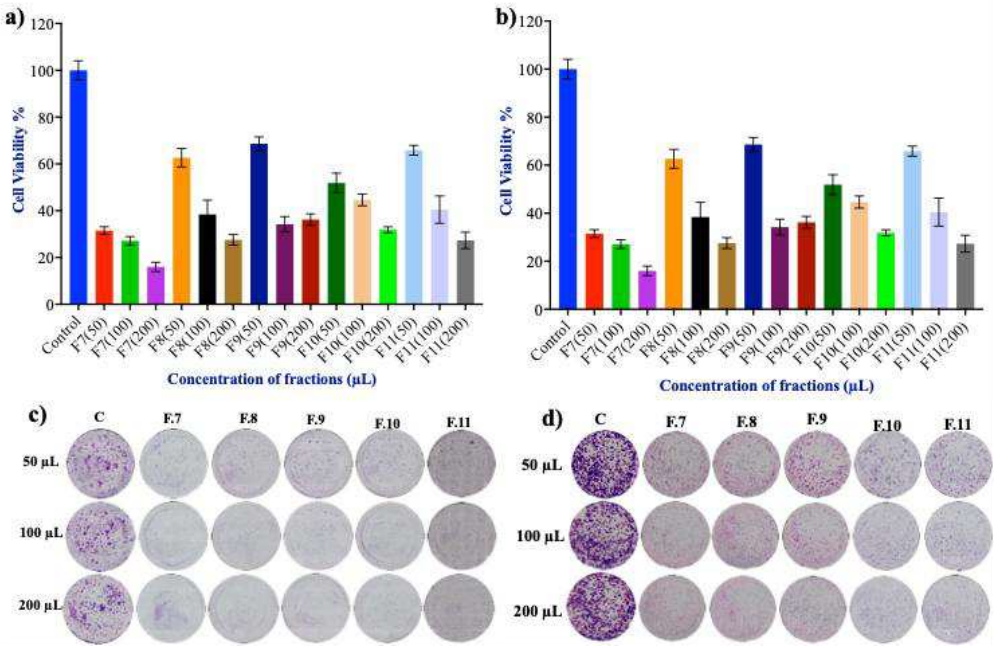


Fig. 6 Cell viability and colony formation assays of BEAS-2B (a, c) and A549 (b, d) cells treated with different fractions (F.7–F.11) of DOX@C-dot at increasing concentrations. Panels (a) and (b) show the percentage of viable cells following one week of treatment. Panels (c) and (d) present representative colony formation images corresponding to each treatment dose (50, 100, and 200 µL), displayed below their respective viability plots. Data represent mean ± SD from three independent experiments**.** Statistical significance determined by one-way ANOVA ($p < 0.0001$).

In contrast, when the same conjugates are applied to BEAS-2B cells, the toxic effects are milder. Even at the highest concentrations used, the cell viability in BEAS-2B cells remains above 60–75% for most fractions and does not further change at higher doses. This disparity underscores the preferential cytotoxicity of the DOX conjugates for the malignant cells, as normal cells are more resistant and retain a higher level of viability throughout the experiments. Overall, these findings emphasize that DOX-based conjugates, especially those further engineered with gold nanoparticle-decorated c-dots (Fig. 7), are far more toxic to lung cancer cells than to normal lung epithelium, suggesting a promising therapeutic window and potential for selective anti-cancer treatment.

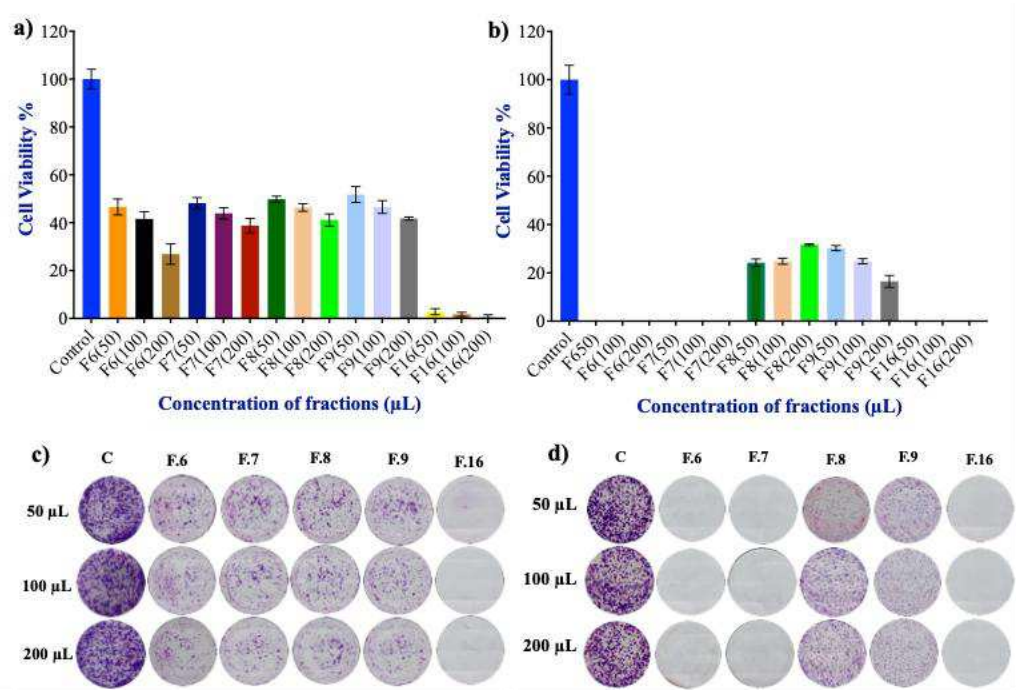


Fig. 7 Cell viability and colony formation assays of BEAS-2B (a, c) and A549 (b, d) cells treated with different fractions (F.7–F.11) of DOX@AuNP@C-dot at increasing concentrations. Panels (a) and (b) show the percentage of viable cells following one week of treatment. Panels (c) and (d) present representative colony formation images corresponding to each treatment dose (50, 100, and 200 µL), displayed below their respective viability plots. Data represent the mean ± SD from three independent experiments. Statistical significance was determined by one-way ANOVA ($p < 0.0001$).

Intracellular localization of DOX@C-dot and DOX@AuNP@C-dot

To assess the intracellular distribution of DOX delivered via DOX@C-dot, fluorescence imaging was performed on A549 and BEAS-2B cells (Fig. 8). The observed red fluorescence emission (represented as counts in the images) is a combined signal having contributions arising from photons emitted by C-dots and DOX. In both cell lines, the red fluorescence was predominantly localized in the cytoplasm, though a portion overlapped with the DAPI-stained nuclei. The colocalization analysis yielded Pearson correlation coefficients of 0.42 in A549 and 0.38 in BEAS-2B cells, indicating partial accumulation of the conjugates in the nuclei. These results suggest that while some nuclear delivery does occur, the overall accumulation of DOX@C-dot within the nucleus is limited. Given DOX's

mechanism of action [21]- DNA intercalation and topoisomerase II inhibition—this distribution pattern may constrain the therapeutic efficacy of the unmodified conjugate [22].

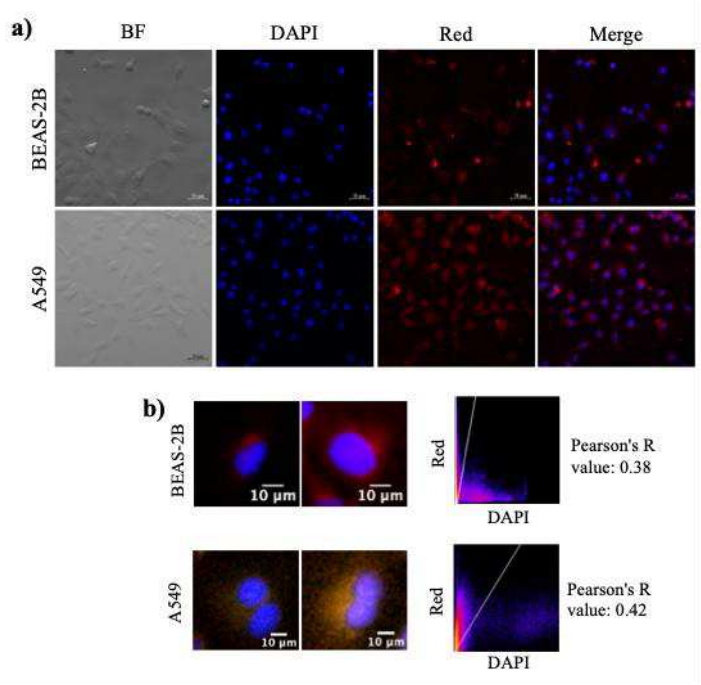


Figure 8. Fluorescence images of BEAS-2B and A549 cells treated with DOX@C-dot. (a) Bright-field (BF), DAPI (nuclear staining), red-channel (DOX@C-dot fluorescence), and merged images for each cell line. (b) Lower panels show representative single-cell images and Pearson's correlation coefficient scatter plots demonstrating the colocalization between DAPI (blue) and DOX@C-dot (red) signals. Pearson's R values were 0.38 for BEAS-2B and 0.42 for A549 cells.

In contrast, the cells treated with DOX@AuNP@C-dots exhibited a marked shift in subcellular localization for the drug-particle conjugates (Fig. 9). In both A549 and BEAS-2B cells, the red fluorescence signal showed greater overlap with nuclear DAPI staining, reflected by higher Pearson correlation coefficients of 0.67 and 0.64, respectively. This suggests that the incorporation of gold nanoparticles significantly enhances nuclear targeting, likely by facilitating cellular uptake and improving intracellular trafficking. Together, these data indicate that the decoration of C-dots with AuNPs improves the efficiency of nuclear delivery—a critical factor for maximizing the therapeutic efficacy of DOX, whose activity relies on DNA intercalation, topoisomerase II inhibition, and ROS generation. These findings establish a strong performance benchmark for the AuNP-decorated drug delivery system and initiate a strong motivation for further optimization toward enhanced nuclear delivery.

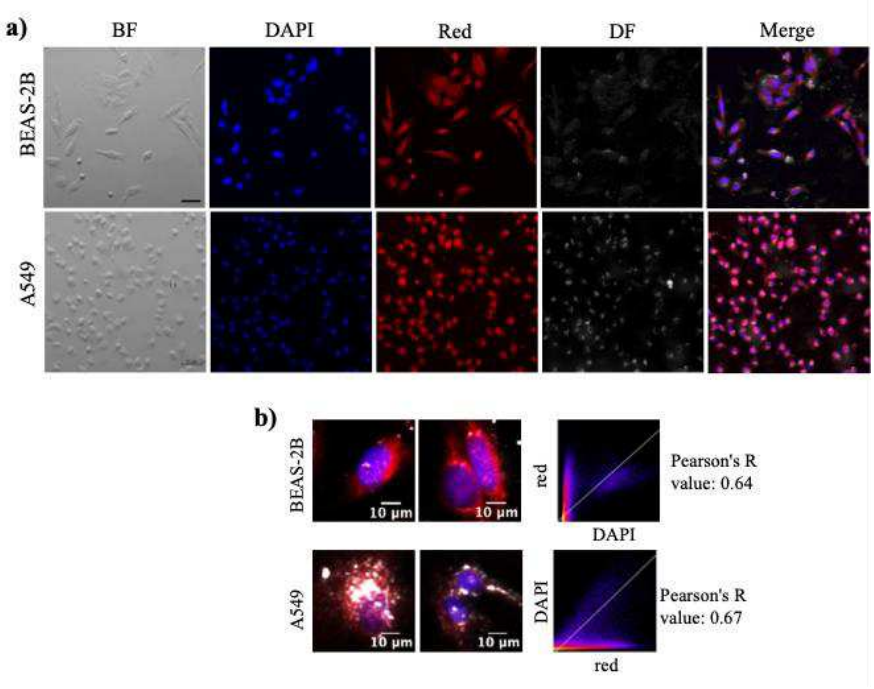


Fig. 9 Fluorescence images and colocalization analysis of BEAS-2B andA549 cells following treatment with DOX@AuNP@C-dot. Imaging and analysis as described in Fig. 8. Pearson's R values of 0.64 (BEAS-2B) and 0.67 (A549) indicate enhanced nuclear colocalization compared to DOX@C-dot (R = 0.38 and 0.42, respectively).

Discussion

The global increase in cancer cases necessitates the development of therapeutic strategies that overcome the inherent limitations of conventional chemotherapy, such as nonspecific targeting, significant off-target toxicity, low cancer selectivity, and insufficient drug accumulation in the tumor tissue. Although DOX remains a cornerstone of clinical cancer therapy, its efficacy is often limited by dose-dependent cardiotoxicity and a narrow therapeutic window [23]. The drug is hampered by poor solubility, non-selective distribution, and significant systemic toxicities. Here, we successfully developed an organic-metal hybrid nanoparticle-based drug delivery platform, AuNP@C-dot, that substantially improves the pharmacological profile of DOX. Our platform enhances cytotoxic potency by 3.2-fold while simultaneously providing 1.7-fold cancer selectivity over normal bronchial epithelial cells. Notably, the fraction F.7 demonstrated exceptional cancer selectivity, achieving killing of 61% cancer cells while causing only 20% normal cell death at the dose of 2.4 µg/mL, corresponding to a 3.1-fold selectivity ratio. These findings demonstrate that the AuNP@C-dot architecture — where C-dot serves as a nuclear-targeting carrier that delivers gold nanoparticles and their drug payload to the nucleus — facilitates superior biodistribution and targeted delivery of the drug-particle conjugate compared with free DOX through improved nuclear access, pH-responsive release, and plasmonic enhancement.

DOX Conjugation

A critical challenge in using DOX is its limited solubility and the difficulty of maintaining stable drug loading. By using a two-step conjugation strategy that first forms a hydrazone bond and then employs EDC/NHS-mediated amide coupling, we achieved a stable covalent attachment of DOX to AuNP@C-dot particles rather than simple physical adsorption. The presence of distinct UV–Vis absorbance bands characteristic of C-dots (~350 nm) and DOX (~480–500 nm) within the same purified chromatographic fractions suggests successful covalent conjugation. Partial quenching of photoluminescence (PL), broadening and red-shifting of the PL band upon DOX attachment further support this conclusion, reflecting π–π stacking interactions and energy transfer between DOX's aromatic rings and the graphitic domains of the C-dots. Notably, the retention of core C-dot fluorescence despite quenching

indicates that conjugation preserves the inherent photoluminescent properties crucial for potential imaging or tracking applications.

Column chromatography successfully separated conjugate-rich fractions that eluted earlier than free species, due to the hydrodynamic size and surface chemistry of the nanocarrier following DOX binding. The diminished DOX absorbance and partial recovery of photoluminescence intensity in later fractions highlight the effective removal of unbound components, confirming that the mid fractions primarily contain stable DOX conjugates. We identified that these mid-range chromatographic fractions provided the most representative conjugate population, balancing effective drug loading (approximately 10–13% DLE) with structural stability and overall mass recovery. Although maximum DLE was achieved in low-mass fractions, the fractions 7–11 offer a suitable compromise between drug payload, nanoparticle stability, and mass recovery, making them ideal for further application studies. This covalent conjugation approach ensures that the drug is protected from non-specific uptake during incubation while remaining available for pH-triggered release in the acidic tumor microenvironment.

Therapeutic Enhancement

The AuNP@C-dot particles exhibited photoluminescence quenching in DOX-rich fractions compared to plain C-dots, suggestive of plasmon-enhanced nonradiative energy transfer or quenching mechanisms. This plasmonic interaction with the AuNP core introduces an additional layer of tunability to the optical response, which could be leveraged for sensitive monitoring of drug release or for theranostic applications. The synergistic combination of carbon and gold nanostructures thus provides both therapeutic enhancement and potential diagnostic capabilities molded in a single platform. The synergistic combination enables radiotherapy through absorption of X-rays by the gold component of AuNP@C-dot, or photodynamic therapy via absorption of visible photons by C-dots, and photothermal treatment localizing heat in the near vicinity of gold. The treatment prospects that could be applied simultaneously or successively offer DOX@AuNP@C-dot drug-nanoparticle conjugate as a great nanomedicine candidate for cancer treatment, but further studies are required.

Quantitative Assessment of Enhanced Cytotoxicity

The biological efficacy of these conjugates was superior to that of free DOX in lung cancer models. Comprehensive IC50 analysis using four-parameter logistic curve fitting revealed that DOX@AuNP@C-dot achieved an IC50 of 1.692 ± 0.633 μg/mL ($R^2 = 0.8161$) in A549 cells, representing a statistically significant 3.2-fold enhancement in potency compared to free DOX. This substantial improvement in cytotoxic efficacy demonstrates that the nanocarrier platform successfully addresses the delivery limitations of conventional doxorubicin therapy. MTT assays demonstrated that DOX@AuNP@C-dot exerted dose-dependent cytotoxic effects on A549, with cytotoxicity directly correlated with the DOX concentration in each fraction. This potency at relatively low concentrations highlights the efficiency of targeted delivery of the gold-decorated C-dot platform.
In contrast, DOX@C-dot showed minimal cytotoxicity across all tested concentrations, with cell viability consistently maintained above 69% and an IC50 that could not be reliably determined within the tested range (>2.4 μg/mL). This difference underscores the synergistic role of the AuNP@C-dot architecture in achieving therapeutic efficacy.

The performance of DOX@AuNP@C-dot is attributed to enhanced nuclear targeting through a unique delivery mechanism: carbon dots serve as nuclear-targeting carriers that transport gold components—which cannot enter the nucleus independently—into the nuclear compartment. Our fluorescence imaging and colocalization analysis revealed that DOX@AuNP@C-dot conjugates were substantially more efficient at reaching the nucleus than DOX@C-dot alone, as established by the Pearson correlation coefficient of 0.67 compared to 0.42, respectively. This greater nuclear delivery (1.6-fold enhancement), enabled by the C-dot carrier function combined with the drug-loading and plasmonic properties of AuNPs, directly correlates with the higher anti-proliferative activity observed.

Comparative Analysis: Benchmarking Hybrid AuNP@C-dot Performance Against Established Nano Delivery Systems

The performance of the DOX@AuNP@C-dot system was evaluated in the context of recent publications on DOX-loaded nanocarriers. Table 4 compares the drug loading efficiencies and cancer cell selectivity indexes of some carbon dot-based carriers reported in the literature with those of the presented system. AuNP and C-dot systems

have each been extensively investigated as independent DOX delivery platforms [24–29] ; their structural combination into a single hybrid nanocarrier is comparatively less common, and we position the present work within that smaller body of literature rather than as an unprecedented strategy. A review of C-dot@noble metal nanoparticle composites by Wang et al. reported sensing, bioimaging, and bacteriostasis as the most frequently pursued applications for such hybrids, with drug delivery represented less often among the reported applications[30]. Recent studies employing CD@AuNP composites have similarly emphasized diagnostic applications, such as multichannel nanosensors for intraoperative cancer malignancy discrimination [31], rather than therapeutic drug delivery. Within this context, the present work contributes a specific combination — structural integration of AuNPs within C-dots for dual drug-binding together with nuclear targeting — that, to our knowledge, has not been reported in combination in the Au-C-dot composite literature we surveyed; we present this as an incremental contribution to that literature rather than a demonstration of a fundamentally new mechanism, and we note that a broader systematic literature search would be needed to confirm how isolated this combination truly is. Our results demonstrate a mean DLE of 11.1% for the pooled active fractions (F7–F10), which represent the stable conjugate population as confirmed by their balanced DOX content and consistent mass ratios.

Table 4. Performance Comparison of DOX Nanocarrier Systems

Nanocarrier System (Source)	Drug Loading Efficiency (DLE %)	Selectivity Index (SI)	IC_{50} Cancer Cell	IC_{50} Normal Cell	Basis for Calculation / Notes
This work: DOX@AuNP@C-dots	11.1%	1.72	1.692 g/mL	2.910 g/mL	Overall SI (IC_{50}-based); a peak fraction-specific selectivity of 3.1-fold was observed at F.7 (2.34 μg/mL), achieving 61% cancer death vs 20% normal cell death
This work: Dox@C-dots	11.0%	1.2	> 2.4 g/mL	> 2.4 g/mL	Pristine system; no significant cancer preference.
Porphyrin CDs [24]	93.0%	~10.9	10.587 mg/mL	> 100 mg/mL	IC50 vs. MDA-MB-231; Normal RPE-1 cells remained >90% viable.
Sucrose CDs [25]	50.0%	> 20.0	~5 mM	> 200 g/mL	Explicitly reported "high discrimination" for renal carcinoma cells.
Milk-derived CDs[29]	87.0%	~10.0	~1.5 M	> 600 g/mL	5% cancer viability (ACC-2) vs. >90% healthy cell viability.
Folic Acid CDs [27]	84.4%	29.8	1.55 g/mL	46.19 g/mL	Ratio between FR+ (targeted) and FR- (low-receptor) cancer cells.
Micellar AuNP [28]	73.2%	4.9	7.94 M	~40 M+	4T1 cancer cells vs. healthy NIH3T3 fibroblast ratio.
γ-Globulin AuNP[26]	28.4%	~10.0	11.87 g/mL	> 42 g/mL	10-fold increase in cytotoxic potency vs. free DOX in glioma cells.

In terms of therapeutic discrimination, the overall Selectivity Index (SI) of 1.72 achieved by DOX@AuNP@C-dot establishes a meaningful therapeutic window compared to the negligible selectivity of pristine C-dots (SI = 1.2) or free DOX (SI ≈ 1.0); at the most selective fraction and concentration tested (F.7, 2.34 μg/mL), this reached a peak of 3.1-fold. Although active targeting platforms, such as Folic Acid-functionalized CDs (SI = 29.8) or organ-specific sucrose CDs (SI > 20), exhibit higher discrimination, our system's overall SI is broadly comparable to established micellar AuNP formulations (SI = 4.9), without the need for complex polymer synthesis or active ligands. Furthermore, the 1.6-fold enhancement in nuclear delivery (Pearson R = 0.67 for AuNP@C-dots vs. 0.42 for C-dots) is a critical performance metric. This identifies our C-dots as effective nuclear-targeting carriers that transport gold clusters and their payload directly to the genomic target site, facilitating superior DNA intercalation compared to free DOX. By balancing practical loading capacity with a competitive selectivity profile, the AuNP@C-dot hybrid provides a clinically relevant therapeutic index and potential for multimodal therapy, offering a promising alternative to traditional single-component nanocarriers.

Cancer Cell Selectivity and Therapeutic Window

The observed preferential cytotoxicity of DOX@AuNP@C-dot toward A549 lung cancer cells compared to BEAS-2B normal lung epithelial cells can be attributed to several synergistic mechanisms inherent to the differential

biology of malignant versus normal cells. Cancer cells typically exhibit elevated endocytic activity driven by their high metabolic demands and accelerated proliferation rates, resulting in enhanced nanoparticle uptake compared to their normal counterparts [21]. Recent studies have demonstrated that cancer cells exhibit up to 30% higher nanoparticle uptake and retention compared to normal cells, with internalization occurring primarily through energy-dependent endocytic pathways, including clathrin-mediated endocytosis and micropinocytosis [22]. Once internalized, the pH-sensitive hydrazone linkage in our conjugate provides an additional layer of selectivity: while the conjugate remains stable at physiological pH (7.4) during circulation and interaction with normal cells, it undergoes rapid hydrolysis in the acidic microenvironment (pH 5.0-6.5), which is characteristically more pronounced in cancer cells due to altered metabolic activity, enhanced glycolysis (Warburg effect), and dysregulated ion transport. This combination of enhanced uptake kinetics and pH-triggered intracellular drug release creates a favourable therapeutic window, allowing DOX@AuNP@C-dot drug-conjugate to achieve selective cancer cell killing while minimizing toxicity to normal epithelial cells.

The marked difference in cancer cell selectivity between DOX@C-dots and DOX@AuNP@C-dots can be rationalized through the structure-activity relationships arising from their distinct molecular architectures and surface chemistries. During the solvothermal synthesis at 240 °C, the pre-formed gold nanoparticles may undergo structural reorganization and partial fragmentation, yielding gold-decorated carbon dot hybrids with comparable dimensions to pristine C-dots (~5.5 nm) but with fundamentally altered surface properties. This transformation creates a heterogeneous nanointerface where gold atoms, clusters, or small nanodomains are intimately embedded within or anchored to the carbonaceous matrix, establishing dual binding sites for DOX conjugation. The presence of gold introduces interaction sites capable of forming coordinate covalent bonds with DOX through multiple mechanisms: (I) electrostatic interactions between positively charged amino groups of protonated DOX and the negatively charged gold surface [23], (II) gold-carbonyl coordination between gold cations ($Au^{\delta+}$) on the nanoparticle surface and the quinone oxygen atoms of DOX [32], and (iii) cation-π interactions [33]. These interactions are distinct from and complementary to the pH-sensitive hydrazone linkages formed at the C-dot surface. This dual-mode conjugation architecture results in a 5-fold enhancement (up to ~220 versus ~46 DOX molecules per particle) in drug loading capacity, creating a higher local drug concentration reservoir that, upon cellular uptake and pH-triggered release, delivers a more therapeutically significant payload. Furthermore, the gold component introduces plasmonic features and enhanced X-ray attenuation that may facilitate secondary therapeutic modalities (radiotherapy and photothermal therapy), while the carbon dot framework maintains intrinsic fluorescence for imaging and provides the nuclear localization sequences that enable direct delivery to the genomic target site, enabling value-added photodynamic therapy. The pristine DOX@C-dots, lacking these gold-mediated effects, demonstrate limited drug loading and correspondingly reduced cancer selectivity, as their smaller payload results in subtherapeutic intracellular concentrations that fail to overcome the apoptotic threshold in cancer cells while still inducing some toxicity in normal cells. Thus, the gold-carbon hybrid nanoarchitecture creates a synergistic platform where structure governs function: the gold domains amplify drug loading and enable multimodal therapy, the carbon matrix provides nuclear targeting and a conjugation site for pH-responsive drug release. This integration results in a drug-carrier system with an improved therapeutic index compared to either component alone.

Limitations

This study has several limitations worth noting. Biological evaluation was performed in a single cancer cell line (A549) alongside one normal line (BEAS-2B), so the selectivity and potency reported here should not yet be generalized beyond this pair without testing in additional lines. Colloidal characterization (DLS, zeta potential, polydispersity) of the unconjugated C-dot and AuNP@C-dot precursors was reported previously [13], but we did not extend these measurements to the DOX-conjugated particles themselves or assess their colloidal stability over time in physiologically relevant media; this would help confirm that conjugation and purification do not alter the particles' behavior in biological fluids. The proposed uptake and nuclear-delivery mechanism is consistent with our colocalization and cytotoxicity data and with established literature on cancer cell endocytosis, but was not directly tested with uptake-pathway inhibitors or flow cytometry, so it should be regarded as a plausible interpretation rather than a confirmed pathway. Finally, all data are from in vitro monoculture; in vivo efficacy, biodistribution, and cardiotoxicity remain to be established. We view these as natural next steps rather than as undermining the present findings, which stand on their own as an in vitro proof-of-concept for the AuNP@C-dot delivery strategy.

Conclusion

This study introduces a particle carrier drug delivery platform, AuNP@C-dot, designed to address specific limitations of conventional doxorubicin therapy. The architecture leverages carbon dots as nuclear-targeting carriers to deliver DOX-loaded gold nanoparticles into the nucleus of A549 lung cancer cells, a mechanism that in this system addresses both the limited drug-loading capacity of C-dots alone and the inability of AuNPs to access nuclear compartments independently. Combined with pH-responsive release and plasmonic enhancement, the AuNP@C-dot platform achieved improved potency and selectivity relative to pristine C-dots and free DOX in the cell lines tested, and the gold component may offer secondary imaging or therapeutic modalities (e.g., X-ray attenuation, photothermal effects) worth exploring in future work. These are in vitro, single-cell-line findings, and we deliberately avoid framing them as evidence of clinical translation potential at this stage. Future investigations should extend testing to additional cancer cell lines, characterize the colloidal stability of the DOX-conjugated particles specifically, directly test the proposed uptake and nuclear-delivery mechanisms, and validate in vivo efficacy, biodistribution, and safety before this platform can be reasonably positioned for clinical development in lung cancer therapy.

Acknowledgments

This work was supported by the Scientific and Technological Research Council of Türkiye (TUBITAK, Project No. 120N526). The manuscript presents part of the findings obtained within the framework of the EURONANOMED Project MATISSE (MoleculAr harvesTing with electroporation and nanoparticles for dIagnoSticS and thErapy of heterogeneous solid tumors, project No. 120). We acknowledge that some spectroscopic measurements were conducted at IYTE-TAM (Integrated Research Centers).

Statements and Declarations

Funding. This work was supported by the Scientific and Technological Research Council of Türkiye (TUBITAK, Project No. 120N526) and the EURONANOMED Project MATISSE (project No. 120).

Competing Interests. The authors have no relevant financial or non-financial interests to disclose.

Ethics Declaration. Not applicable.

Data Availability. All data that support the findings of this study are included within the article (and any supplementary files).

Author Contributions. I.S. and S.Ö. contributed to the study conception and design. Material preparation, data collection, and analysis were performed by I.S. The first draft of the manuscript was written by I.S., and both authors commented on previous versions of the manuscript. Both authors read and approved the final manuscript.

References

1. Giri PM, Banerjee A, Layek B (2023) A Recent Review on Cancer Nanomedicine. Cancers 15:. https://doi.org/10.3390/CANCERS15082256

2. Rahman MA, Jalouli M, Yadab MK, Al-Zharani M (2025) Progress in Drug Delivery Systems Based on Nanoparticles for Improved Glioblastoma Therapy: Addressing Challenges and Investigating Opportunities. Cancers 2025, Vol 17, Page 701 17:701. https://doi.org/10.3390/CANCERS17040701

3. Bhadran A, Polara H, Babanyinah GK, Baburaj S, Stefan MC (2025) Advances in Doxorubicin Chemotherapy: Emerging Polymeric Nanocarriers for Drug Loading and Delivery. Cancers 2025, Vol 17, Page 2303 17:2303. https://doi.org/10.3390/CANCERS17142303

4. Amin MS, Rahman A, Prapty AN, Numan AA, Rahman MM, Ahmed B, Shabuj MMH, Aunni SAA (2024) Nanomedicine in Cancer Therapy: From Preclinical Promise to Clinical Applications. Journal of Precision Biosciences 6:1–14. https://doi.org/10.25163/BIOSCIENCES.6110064

5. Ramayanam NR, Bukke SPN, Moka MK, Dehingia H, Bordoloi A, Debbarma R, Kudumula PR, Vuyyala B, Prasad PD, Catherine A (2025) Advances in nanoparticle-based doxorubicin delivery: precision strategies for targeted treatment of triple-negative breast cancer. Discover Nano 20:111. https://doi.org/10.1186/S11671-025-04308-5

6. Theivendren P, Kunjiappan S, Pavadai P, Ravi K, Murugavel A, Dayalan A, Santhana Krishna Kumar A (2024) Revolutionizing Cancer Immunotherapy: Emerging Nanotechnology-Driven Drug Delivery Systems for Enhanced Therapeutic Efficacy. ACS measurement science au 5:31–55. https://doi.org/10.1021/ACSMEASURESCIAU.4C00062

7. Tian M, Liu X, Pei H (2024) Nanomaterial-based cancer immunotherapy: enhancing treatment strategies. Frontiers in Chemistry 12:1492215. https://doi.org/10.3389/FCHEM.2024.1492215/BIBTEX

8. Gayathri K, Vidya R (2024) Carbon nanomaterials as carriers for the anti-cancer drug doxorubicin: a review on theoretical and experimental studies. Nanoscale Advances 6:3992–4014. https://doi.org/10.1039/D4NA00278D

9. Xia W, King MW (2025) Advances in Targeted Delivery of Doxorubicin for Cancer Chemotherapy. Bioengineering 12:430. https://doi.org/10.3390/BIOENGINEERING12040430

10. Ibrahim AA, Nsairat H, Al-Sulaibi M, El-Tanani M, Jaber AM, Lafi Z, Barakat R, Abuarqoub DA, Mahmoud IS, Obare SO, Aljabali AAA, Alkilany AM, Alshaer W (2024) Doxorubicin conjugates: a practical approach for its cardiotoxicity alleviation. Expert Opinion on Drug Delivery 21:399–422. https://doi.org/10.1080/17425247.2024.2343882

11. Zeng W, Luo Y, Gan D, Zhang Y, Deng H, Liu G (2023) Advances in Doxorubicin-based nano-drug delivery system in triple negative breast cancer. Frontiers in Bioengineering and Biotechnology 11:1271420. https://doi.org/10.3389/FBIOE.2023.1271420/FULL

12. Yang L, Wang Z, Wang J, Jiang W, Jiang X, Bai Z, He Y, Jiang J, Wang D, Yang L (2016) Doxorubicin conjugated functionalizable carbon dots for nucleus targeted delivery and enhanced therapeutic efficacy. Nanoscale 8:6801–6809. https://doi.org/10.1039/C6NR00247A

13. Kavuranpala T, Saydullaeva I, Özçelik S (2025) Developing gold nanoparticles decorated with carbon-dots for multiplexed cellular imaging. Nanotechnology 36:445102. https://doi.org/10.1088/1361-6528/ae1508

14. Hettiarachchi SD, Kirbas Cilingir E, Maklouf H, Seven ES, Paudyal S, Vanni S, Graham RM, Leblanc RM (2021) Advances in Doxorubicin-based nano-drug delivery system in triple negative breast cancer. Nanoscale 13:5507–5518. https://doi.org/10.1039/d0nr08381j

15. Hettiarachchi SD, Graham RM, Mintz KJ, Zhou Y, Vanni S, Peng Z, Leblanc RM (2019) Triple conjugated carbon dots as a nano-drug delivery model for glioblastoma brain tumors. Nanoscale 11:6192–6205. https://doi.org/10.1039/C8NR08970A

16. Cailotto S, Mazzaro R, Enrichi F, Vomiero A, Selva M, Cattaruzza E, Cristofori D, Amadio E, Perosa A (2018) Design of Carbon Dots for Metal-free Photoredox Catalysis. ACS Applied Materials and Interfaces 10:40560–40567. https://doi.org/10.1021/acsami.8b14188

17. Su L, Rezaei S, Mejia G, Pandey P, Dit Fouque KJ, Fernandez-Lima F, McGoron A, He J, Leng F (2024) Conjugating Daunorubicin and Doxorubicin to GTP by Formaldehyde to Overcome Drug Resistance. ChemMedChem 19:e202300481. https://doi.org/10.1002/CMDC.202300481

18. Carney RP, Kim JY, Qian H, Jin R, Mehenni H, Stellacci F, Bakr OM (2011) Determination of nanoparticle size distribution together with density or molecular weight by 2D analytical ultracentrifugation. Nature Communications 2011 2:1 2:335-. https://doi.org/10.1038/ncomms1338

19. Punia R, Raina K, Agarwal R, Singh RP (2017) Acacetin enhances the therapeutic efficacy of doxorubicin in non-small-cell lung carcinoma cells. PLoS ONE 12:1–19. https://doi.org/10.1371/journal.pone.0182870

20. Kashkin KN, Musatkina EA, Komelkov AV, Favorskaya IA, Trushkin EV, Shleptsova VA, Sakharov DA, Vinogradova TV, Kopantzev EP, Zinovyeva MV, Kovaleva OV, Zborovskaya IB, Tonevitsky AG, Sverdlov ED (2010) Expression profiling and putative mechanisms of resistance to doxorubicin of human lung cancer cells. Doklady Biochemistry and Biophysics 430:20–23. https://doi.org/10.1134/S1607672910010072

21. Chan ET, Kural C (2024) Targeting endocytosis to sensitize cancer cells to programmed cell death. Biochemical Society Transactions 52:1703. https://doi.org/10.1042/BST20231332

22. Bromma K, Bannister A, Kowalewski A, Cicon L, Chithrani DB (2020) Elucidating the fate of nanoparticles among key cell components of the tumor microenvironment for promoting cancer nanotechnology. Cancer Nanotechnology 11:8. https://doi.org/10.1186/S12645-020-00064-6

23. Mirza AZ, Shamshad H (2011) Preparation and characterization of doxorubicin functionalized gold nanoparticles. European Journal of Medicinal Chemistry 46:1857–1860. https://doi.org/10.1016/J.EJMECH.2011.02.048

24. Ansary A, Osman A, El-Khouly ME (2025) Doxorubicin-loaded pH-responsive porphyrin-derived carbon dots as a promising biocompatible drug delivery system for effective chemotherapy of breast cancer. RSC Advances 15:6457–6473. https://doi.org/10.1039/D4RA09058F

25. Azmi F, Xu X, Duong H, Ye P, Chen T, Li H, Chen J, Ardekani SM, Dehghani A, Zheng G, Harris D, Lu H, Wang Y, Cao Q (2025) Renal clearable sucrose carbon dots for doxorubicin delivery to treat renal carcinoma. Nanoscale Advances 7:2751–2760. https://doi.org/10.1039/d4na01082e

26. Chauhan G, Chopra V, Alvarado AG, Gómez Siono JA, Madou MJ, Martinez-Chapa SO, Kulkarni MM (2024) Doxorubicin Conjugated γ-Globulin Functionalised Gold Nanoparticles: A pH-Responsive Bioinspired Nanoconjugate Approach for Advanced Chemotherapeutics. Pharmaceutics 16:. https://doi.org/10.3390/PHARMACEUTICS16020208

27. Dada SN, Babanyinah GK, Tetteh MT, Palau VE, Walls ZF, Krishnan K, Croft Z, Khan AU, Liu G, Wiese TE, Glotser E, Mei H (2022) Covalent and Noncovalent Loading of Doxorubicin by Folic Acid-Carbon Dot Nanoparticles for Cancer Theranostics. ACS Omega. https://doi.org/10.1021/acsomega.2c01482

28. Dyagala S, Paul M, Das S, Halder S, Biswas S, Saha SK (2025) Targeted Phototriggered and pH-Responsive Micellar Cancer Drug Delivery System with Real-Time Monitoring through the NSET Mechanism. ACS Applied Bio Materials 8:9680–9695. https://doi.org/10.1021/ACSABM.5C00770

29. Yuan Y, Guo B, Hao L, Liu N, Lin Y, Guo W, Li X, Gu B (2017) Doxorubicin-loaded environmentally friendly carbon dots as a novel drug delivery system for nucleus targeted cancer therapy. Colloids and Surfaces B: Biointerfaces 159:349–359. https://doi.org/10.1016/j.colsurfb.2017.07.030

30. Wang X, Ma M, Zhang T, Ma Y, Ma X, Shi F, Zhang R, Xu Z (2024) Carbon dots@noble metal nanoparticle composites: research progress report. The Analyst 149:. https://doi.org/10.1039/d3an01580g

31. Xiao Y, Peng B, Zhu X, Long Y, Liu F, Liu M, Li H, Zhang Y, Yao S (2025) Machine learning-assisted multichannel nanosensor based on core-shell carbon dot/gold nanoparticle composites for rapid and precise intraoperative oral cancer malignancy diagnosis. Sci China Chem 68:5273–5283. https://doi.org/10.1007/s11426-025-2678-6

32. Curry D, Cameron A, MacDonald B, Nganou C, Scheller H, Marsh J, Beale S, Lu M, Shan Z, Kaliaperumal R, Xu H, Servos M, Bennett C, MacQuarrie S, Oakes KD, Mkandawire M, Zhang X (2015) Adsorption of

doxorubicin on citrate-capped gold nanoparticles: insights into engineering potent chemotherapeutic delivery systems. Nanoscale 7:19611–19619. https://doi.org/10.1039/C5NR05826K

33. Du Y, Xia L, Jo A, Davis RM, Bissel P, Ehrich MF, Kingston DGI (2018) Synthesis and Evaluation of Doxorubicin-Loaded Gold Nanoparticles for Tumor-Targeted Drug Delivery. Bioconjugate Chemistry 29:420–430. https://doi.org/10.1021/ACS.BIOCONJCHEM.7B00756

Supplementary Files

This is a list of supplementary files associated with this preprint. Click to download.

- SupportingMaterials.docx